Structural and magnetic properties of high magnetization Fe_xCo_{100-x} nanoparticles investigated at the nanoscale: Unveiling the origin of the observed anisotropy

Jon Gutiérrez [a,b,*], Virginia Vadillo [b,1], Inés Puente [c,d], Claudia Mondelli [e], Marie Capron [f], Javier Alonso [g], Iñaki Orue [h], Patricia Lázpita [a,b], Joseba S. Garitaonandia [a,b], Izaskun Gil de Muro [a,b], Tommaso Baroni [i], Francesco D'Acapito [j], Maite Insausti [a,b]

[a] Faculty of Science and Technology, Universidad del País Vasco/Euskal Herriko Unibertsitatea, Barrio Sarriena s/n, Leioa 48940, Spain
[b] BCMaterials (Basque Center for Materials, Applications & Nanostructures), UPV/EHU Scientific Park, Bldg. Martina Casiano, 3rd. Floor, Barrio Sarriena s/n, Leioa 48940, Spain
[c] Institut Laue Langevin, 71 Avenue des Martyrs, CS 20156, Grenoble Cédex 38042, France
[d] Instituto de Nanociencia y Materiales de Aragón, CSIC-Universidad de Zaragoza, Pedro Cerbuna 12, Zaragoza 50009, Spain
[e] CNR-IOM, Institut Laue Langevin, 71, Avenue des Martyrs, Grenoble Cédex 38042, France
[f] European Synchrotron Radiation Facilities (ESRF), 71 Avenue des Martyrs, CEDEX 9, Grenoble 38042, France
[g] CITIMAC Department, Universidad de Cantabria, Santander 39005, Spain
[h] SGIKER, Universidad del País Vasco/Euskal Herriko Unibertsitatea, Barrio Sarriena s/n, Leioa 48940, Spain
[i] Department of Earth Sciences, University of Florence, via La Pira 4, Firenze 50121, Italy
[j] CNR-IOM-OGG c/o ESRF-The European Synchrotron, 71 Avenue des Martyrs, CS 40220, Grenoble Cédex 38043, France

ARTICLE INFO

ABSTRACT

In this work the authors have performed the synthesis of Fe_xCo_{100-x} (0<x<100) alloy nanoparticles (NPs) with different compositions, as well as pure Fe and Co NPs for comparison, by a chemical reduction technique. The subsequent characterization demonstrated excellent quality NPs with the expected bcc cubic (for Fe and FeCo alloys) and hcp hexagonal (for Co NPs) structures showing a room temperature magnetization as high as 235 emu/g for the $Fe_{66}Co_{34}$ composition alloy. Nevertheless, this soft magnetic character is accompanied by determined values of effective anisotropy as high as 2 MJ/m³. Aiming to deep into the properties of these FeCo alloys as well as to unveil the origin of that observed high anisotropy value, we now present an extensive study at the nanoscale of the synthesized Fe, Co and Fe_xCo_{100-x} alloy nanoparticles by using nuclear techniques as neutron powder diffraction, EXAFS and XANES spectroscopies. Mössbauer spectroscopy revealed that the FeCo alloys are in an A2 disordered solid solution. The obtained results, combined with AFM/MFM images, have demonstrated that despite the cubic bcc structure observed for all FeCo alloys (in excellent concordance with the pure Fe one) the NPs show a "flaky" shape of 50–60 nm size (diameter) but only 3–4 nm thickness, giving rise to a strong shape anisotropy contribution to the observed total effective anisotropy.

1. Introduction

Magnetic nanoparticles (MNPs) are nowadays a key class of materials that has contributed very quickly to the improvement and development of applications in the nanotechnology field [1–3]. They can be obtained in the size range from a few to 100 nm, and due to their unique properties they are being widely used in fields like biomedicine (superparamagnetic Fe_3O_4 and Fe_2O_3 particles due to their biocompatibility can be applied in magnetic targeting or magnetic resonance imaging, MRI [4]), heat release (like AC excitation magnetic field of a magnetic fluid for hyperthermia [5]) or in catalysis applications (since Fe, Co, Ni and their alloy component metals as Pt and Pd are catalytically active [6]).

Apart from those previously mentioned compositions, the FeCo alloy

belongs to the group of soft ferromagnetic materials with the highest known magnetization (about 235 emu/g for a 35 %wt of Co content), large permeability, low coercivity, and high Curie temperature (about 1000 K) [7]. The actual trend is also to fabricate this material at the "nano" scale [8–11], where the outstanding magnetic properties of this FeCo alloy make possible to extend applications of MNPs to magnetic recording media [12], exchange-coupled nanocomposite magnets [13] or also smart fluids [14].

In a previous work [15] we have presented the synthesis (by a chemical reduction method) and characterization at the macroscopic scale of three Fe_xCo_{100-x} (x = 66, 51 and 33) alloy nanoparticles (NPs). Briefly, all of them show bcc cubic structure like the parent Fe powder also synthesized following the same procedure; they show room temperature magnetization values (at 1,5 T applied magnetic field) over 200 Am^2/kg and coercive field values in the range 5–6.5 kA/m. But despite this soft magnetic character exhibited by these FeCo compositions, they also show unexpected magnetic anisotropy values as high as 2 MJ/m^3. This value turns out to be in clear contrast with the magnetic anisotropy for $Fe_{50}Co_{50}$ bulk alloy, about 15–20 kJ/m^3 [16].

It is already well stablished that magnetic properties shown by nanostructured magnetic materials are different if compared with the same parent composition at the bulk state. In this last, magnetism arises from electronic spin-spin and spin-orbit as well as exchange interactions of free electrons. Reducing material dimensions to the nanoscale leads to a confinement of electronic interactions, and as a first consequence magnetic performance (reflected in magnetic saturation, permeability and remanence) becomes size-dependent. When using MNPs for any particular application, the role of magnetic anisotropy arises as a capital question [17]. Many properties of magnetic nanoparticles like the initial magnetic susceptibility or temperature-dependent magnetic relaxation, when used for applications, depend to a great extent on the magnetic anisotropy [18].

Aiming to deep into the properties of these FeCo alloys as well as to unveil the origin of the observed high anisotropy value, in the following we will report a deep study performed at the nanoscale, by using microscopic techniques as neutron powder diffraction (NPD), transmission electron (TEM) and atomic/magnetic force (AFM/MFM) microscopies, X-ray Absorption (XAS) and Mössbauer spectroscopies.

XAS (for our purposes Extended X-ray Absorption Fine Structure, XANES, and X-ray Absorption Near Edge Structure, EXAFS, spectroscopies) is a local-structure sensitive and element specific technique [19] based on the measurement of the variation of the absorption coefficient as a function of the applied X-ray energy. It can provide important information about the phase distribution inside a sample, the relative oxidation state, so as quantitative data on the nature of the ligands and the interatomic distances between a central atom and its neighbors. Due to its properties, XAS perfectly complements the long-range information coming from XRD analysis [19]. The possibility to study separately Fe and Co atoms environment will allow us to determine the correct formation of FeCo alloy nanoparticles, providing evidences on the structural homogeneity of the samples or the segregation of Fe- or Co-rich regions.

The combination of such powerful techniques will give a clear insight mainly in the structure and morphology of the synthesized Fe, Co and FeCo nanoparticles, with emphasis on the assessment of their composition and atomic order/disorder characteristics.

2. Experimental

2.1. Preparation of the Fe_xCo_{100-x} nanoparticles

Different composition Fe_xCo_{100-x} nanoparticles were synthesized by employing a chemical reduction route: pure Fe (x=100), Fe_xCo_{100-x}: Fe excess (x/(100-x) > 1), FeCo: equiatomic (x/(100-x) = 1), Fe_xCo_{100-x}: Co excess (x/(100-x) < 1) and pure Co (x = 0). Three of the synthesized compositions belong to the FeCo binary alloy, and in the following these

NPs will be labelled as Fe, Fe_{exc}Co, FeCo, $FeCo_{exc}$ and Co, respectively.

Briefly, in the chemical reduction method employed, aluminium powder was used to reduce Fe (III) and Co (II) precursors in the presence of NH_4F. By using the same chemical procedure, pure Fe and Co nanoparticles were also synthesized. Extensive information about used products, quantities and the preparation method for all the synthesized compositions can be found in the Supplementary Material (S1 in SM).

2.2. TEM and AFM/MFM microscopy characterization

Morphology of the raw powder of all synthesized compositions was first analyzed by Transmission Electron Microscopy (TEM) technique. TEM images were obtained using a Philips CM200 microscope at an acceleration voltage of 200 kV. Observation samples preparation was performed by using Fe, Co and FeCo alloy nanoparticles with different compositions dispersed in hexane and drop-casted onto a copper grid. To estimate the nanoparticles (or their agglomerates) size, ImageJ software was used [20].

A deeper insight to our nanoparticles morphology was achieved from AFM images obtained by using a fast scanning an Asylum Research Cypher-S instrument provided by the ESRF through the Partnership for Soft Condensed Matter (PSCM). The imaging was performed at room temperature (295 K) in Magnetic Force Microscopy (MFM) mode. Magnetic force microscope (MFM) is a powerful non-contact tool for characterizing sub-micrometer magnetic domains [21]. This technique is complementary to TEM observations for the morphological analysis because it is sensitive to the thickness of the nanoparticles, an important characteristic as it will be further discussed. The AFM was equipped with Asylum Research's ASYMFMHC-R2 probes with a spring constant of 3.3 Nm and a typical resonance frequency of 74.5 kHz, determined via the thermal noise method. The nominal tip radius is 32 nm, while its magnetic tip coating is CoCr. The scan rate was 1.5 Hz. Samples for this technique were prepared by depositing on a clean mica surface one drop of nanoparticles in ethanol suspension, with subsequent drying by spin coating process running at 30,000 rpm for 60 seconds.

2.3. Neutron powder diffraction

Neutron Powder Diffraction (NPD) patterns of our NPs were measured at the diffractometer D1B, ILL (Institut Laue-Langevin, France) using an Orange Cryostat. Wavelength was refined to λ = 1.2863 Å. Diffraction data were continuously collected from 10 to 300 K while temperature changed at a rate of 0.5 K/min. The measurements were performed between $20°$ and $140°$ in 2θ with steps of $0.1°$. The measured peak shape was modeled with a modified Thompson-Cox-Hasting pseudo-Voigt function with axial divergence asymmetry. The crystal structure was refined using the Rietveld method [22] implemented in the FULLPROF program [23]. Measured data set can be found in [24].

2.4. X-ray absorption data collection (XANES and EXAFS)

Complementary to Neutron Powder Diffraction (NPD) technique that reveals information on the average structure of the alloy, the X-ray absorption spectroscopy (XAS) offers the possibility to study separately Fe and Co atoms environment and allows to prove the correct formation of FeCo alloy nanoparticles as well as the presence of non-desired phases, like Fe- or Co- oxides. Thus, a detailed study on our synthesized Fe, Co and FeCo alloy nanoparticles was performed by means of XAS measurements made in two different regions: the near edge structure (XANES) and the extended fine structure (EXAFS). Room temperature measurements were performed at the BM-08 "LISA" CRG Beamline at the European Synchrotron Radiation Facility (ESRF) in Grenoble, France [25]. Data were collected at the Fe (7112 eV) and Co (7709 eV) K edges using Si (111) crystals in the monochromator. The samples were measured at 10 K through the use of a cold-finger liquid-He cryostat.

Higher harmonics rejection is obtained through Si coated collimating/focusing mirrors (with $E_{cutoff} \approx 15keV$). Spectra were acquired in transmission mode with a fixed 5 eV step in the pre-edge region, 0.5 eV step around the edge and a k step of 0.05 Å^{-1} up to a maximum value of $k_{max} = 17$ Å^{-1} for the Co spectra and $k_{max} = 12.5$ Å^{-1} for the Fe ones due to the co-presence of Co. Up to 4 consecutive scans per sample were acquired in order to improve the signal-to-noise ratio. The samples were prepared by mixing the Fe, Co or FeCo alloy powders with 50 mg of cellulose, in order to keep the total absorption μ<1.5, and afterwards they were pressed in pellets.

Together with our study samples, Fe₃O₄ (magnetite) CoFe₂O₄ and Co₃O₄ oxides were also analysed in order to verify the presence of oxides in the FeCo alloys structure. Finally, spectra of Fe and Co foils were also measured simultaneously as references and for data analysis purposes in order to monitor possible energy shifts during consecutive data acquisitions.

2.5. SQUID magnetometry and Mössbauer spectroscopy

Magnetic properties were measured by using a superconducting quantum interference device magnetometer (SQUID, Quantum Design MPMS-5) both at room (300 K) and low (5 K) temperatures, by applying a magnetic field up to 5 Tesla (about 4 MA/m). On the other hand, our FeCo alloys order at the atomic scale was analysed by using Mössbauer spectroscopy. Room temperature spectra were measured in transmission geometry by using a ^{57}Co–Rh source and conventional constant-acceleration spectrometer. Isomer shift values were calculated with respect to an α-Fe calibration foil. NORMOS program develop by Brand [26] was used for fitting the spectra.

3. Results and discussion

In all the synthesized alloy samples, the Fe/Co ratio estimated from different experimental techniques is slightly lower than the initially expected one from the nominal ratio of 1.25:0.5, 1:0.75 and 0.7:1.05 of Fe:Co precursors respectively used for the synthesis (see Supplementary Material). Besides, a small amount of aluminium appears as impurity (in the range 0.3–0.5 %at). This is a direct consequence of an excess of aluminium added to the reaction in order to increase the yield of the chemical reduction process. Nanoparticles compositions were firstly determined by Inductively Coupled Plasma-Mass Spectroscopy, ICP, giving as result Fe$_x$Co$_{100-x}$ alloys with x = 66, 51 and 33 compositions [15] (see Table 1).

TEM images (see Fig. 1) reveal that all the obtained Fe, Co and FeCo alloy powders are composed of single nanoparticles ranging in a size from 20 to 80 nm and irregular shape, but that easily agglomerate forming in many cases dendritic-like structures as big as 600 nm. These NPs clusters appear due to the high dipolar interactions among the magnetic nanoparticles. Crystallite sizes calculated from neutron powder diffraction data confirm these estimations (Table S2).

AFM/MFM images were obtained for nanoparticles set on a flat, non-magnetic mica surface. In Fig. 2a negative phase shift is observed because of the attractive magnetic force of the single FeCo nanoparticle.

In the corresponding topography image of the same particle (Fig. 2b), the individual magnetic particle can be observed, showing a good correlation between the MFM and AFM response. From the line profile across the white line marked of the single nanoparticle, the domain size has been estimated in 24 nm, which is slightly smaller than that obtained from XRD data (see Table S1). Note that the side shoulders on the figure are an experimental artifact due to a thin layer of water coming from the humidity present in the air. The 2–3 nm thickness observed in the AFM/MFM images reveals the "flaky" shape of the nanoparticle. All the single particles that have been found, have been checked and this planar shape has been corroborated.

Due to the strong magnetic moment of each single NP, as it will be showed in the next sections, nanoparticles easily agglomerate forming clusters as big as 500 nm, but with thicknesses not over 12 nm, unveiling for agglomerates of 3–4 layers of single NPs (Fig. 3). The profile along the white line of the topographical image of Fig. 3b shows an agglomerate of magnetic domains ranging from 20 nm to 60 nm size, in agreement with TEM observations.

Fig. 4 shows the obtained room temperature neutron diffraction patterns of all the studied samples. For pure Co, the synthesized nanoparticles show a hexagonal structure (P6₃/mmc) with cell parameters $a = 2.5098 \pm 0.0005$ Å and $c = 4.08530 \pm 0.0003$ Å. The pure Fe powder diffraction pattern shows the expected peaks ((110) at 37.06°, (200) at 53.54°, (211) at 67.00°, (220) at 79.23°, (310) at 90.98°, (222) at 102.70° and (321) at 114.45°) of the α-bcc structure with Im-3m space group and cell parameter $a = 2.8658 \pm 0.0002$ Å (see Table 1).

Like Fe NPs, the structures of the FeCo alloy nanoparticles match also well with the α-bcc structure (S.G. Im-3m), despite the slightly displacement of the diffraction peaks to higher 2θ values. That is, the cell parameter decreases as the amount of iron decreases, from $a = 2.8617$ (3) Å for the Fe$_{exc}$Co alloy to $a = 2.8422(4)$ Å for the FeCo$_{exc}$ one (see Table 1). On the other hand, the values determined for our cell a parameter are in good agreement with cell parameter values previously obtained by other authors in FeCo alloy nanoparticles synthesized by other chemical routes [27,28] but also to other kind of morphologies as FeCo films where Fe/Co ratio progressively varies [29] or those reported for bulk species [30]. In the case of bulk alloys, despite the tendency is maintained, lattice parameters values are slightly higher than those from nanocrystalline samples [28].

Measured neutron diffraction spectra at 10 K are similar to those observed at room temperature. Fig. 5 shows the temperature dependence of the lattice parameters between 10 and 300 K. Cell parameters obtained at 10 K appear in Supplementary Material, together with calculated crystallite sizes (Table S2). For the Fe and FeCo alloys, there is no evident change up to temperatures around 100 K, followed by a smooth, monotonic linear increase of the lattice parameter with temperature up to 300 K. The lattice parameters of Co nanoparticles show a similar behaviour but with a "plateau" in the values measured up to 120 K.

This trend agrees with the one expected for a material without a structural phase transition, as it is our case with all the studied samples. From obtained data, we can estimate the linear thermal expansion coefficient α at high temperatures (from T > 100 K for Fe and FeCo alloys

Table 1

Samples compositions (expected and estimated from ICP analysis), room temperature lattice parameter values, slope of their change with temperature and calculated linear thermal expansion coefficient obtained by NPD measurements, for Fe, Fe$_x$Co$_{100-x}$ and Co synthesized nanoparticles.

| Sample label	Sample nominal composition	Synthesized powder composition*	R.T. lattice parameter a (Å)	slope (x10^{-5} Å/K) at high temperature	α (x10^{-6} K^{-1}) at high temperature
Fe	Fe	Fe	2.8658 ± 0.0002	2.489	8.84
Fe$_{exc}$Co	Fe$_{71}$Co$_{29}$	Fe$_{66}$Co$_{34}$	2.8617 ± 0.0003	2.453	8.85
FeCo	Fe$_{57}$Co$_{43}$	Fe$_{51}$Co$_{49}$	2.8527 ± 0.0004	2.608	8.18
FeCo$_{exc}$	Fe$_{40}$Co$_{60}$	Fe$_{33}$Co$_{67}$	2.8422 ± 0.0004	2.559	7.98
Co	Co	Co	a = 2.5098 ± 0.0005	1.549	5.84
			c = 4.0853 ± 0.0002	2.559	21.9

(*) estimated by using ICP technique.
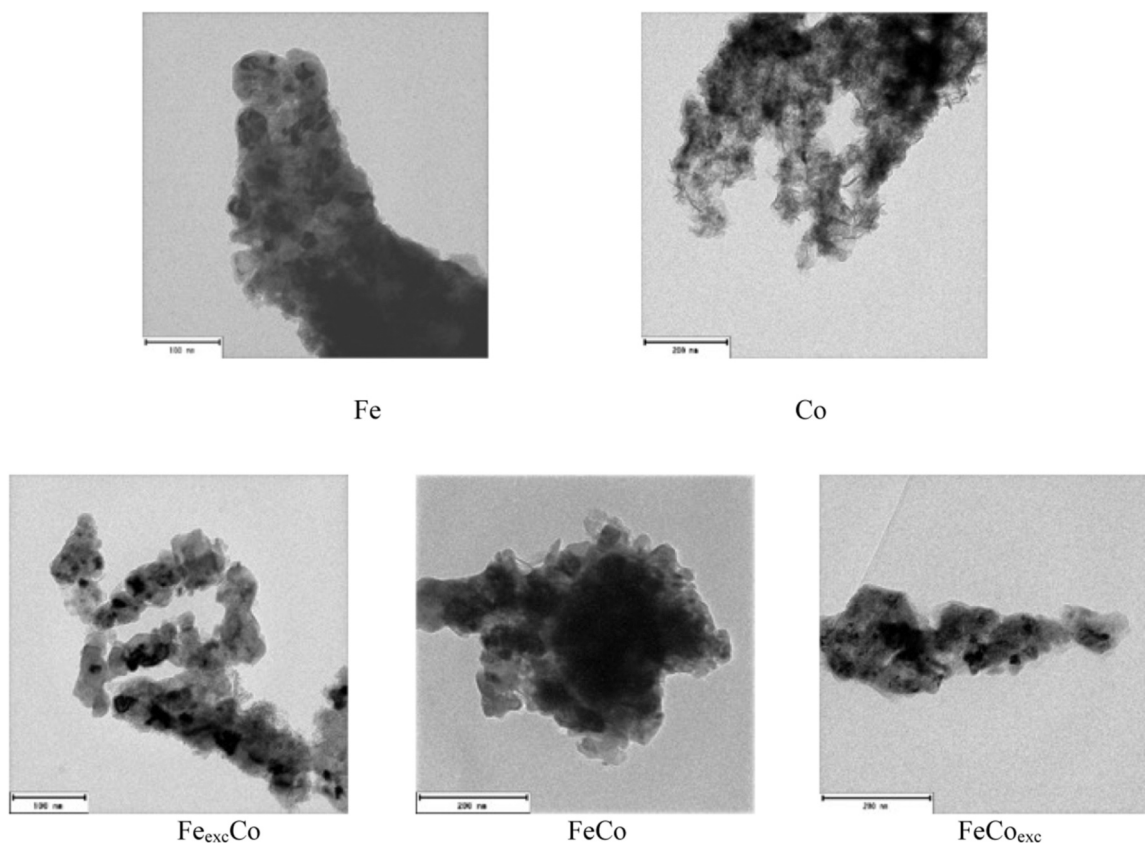
Fig. 1. TEM images of the raw powder of Fe, Co and FeCo alloys synthesized by the chemical reduction method.
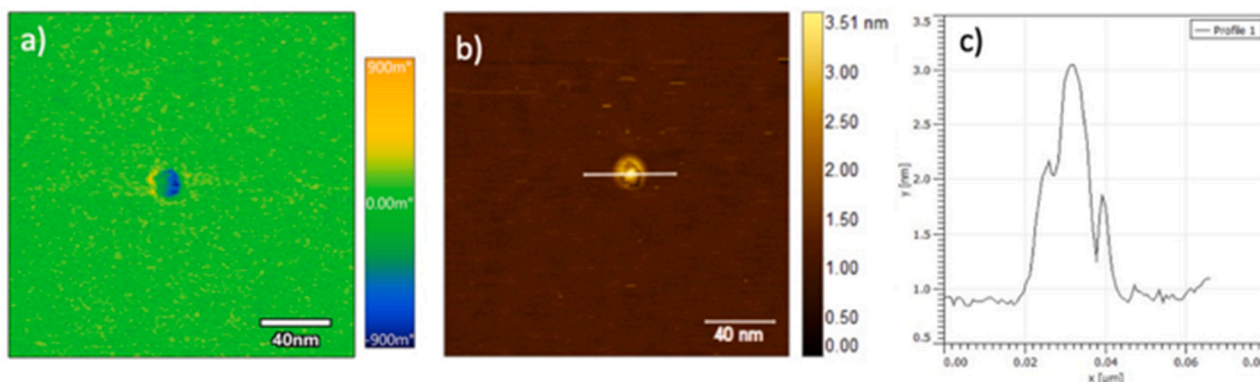

Fig. 2. a) MFM phase shift image of a single nanoparticle of the $FeCo_{exc}$ alloy and b) its corresponding topographical image; c) nanoparticle profile along the white line marked in b).

or from 120 K for the Co nanoparticles) as $\alpha = \frac{1}{a_0} \frac{\Delta a}{\Delta T}$ (where a_0 is the lattice parameter at $T_0 = 300$ K). Thus, the estimated thermal expansion coefficients α range from 8.85 (Fe and Fe-rich FeCo alloy) to 7.98×10^{-6} K^{-1} for the Co-rich alloy (see Table 1). These values are slightly lower than coefficients for pure bulk Fe and Co, with values about 10–12×10^{-6} K^{-1}, but this decrease in these coefficients between bulk and nanocrystalline phase of the material has been already observed, for example for Fe [31]. Moreover, our observations are in good agreement with theoretical predictions done in FeCo alloys about those slopes with values of 9.6×10^{-6} K^{-1} [32] and 10.17×10^{-6} K^{-1} [33].

In a solid, thermal expansion is caused by anharmonic terms in the interaction / restoring potential between individual atoms / molecules. For metals (as our Fe, FeCo alloys, and Co NPs are) at low temperatures, the dominant temperature dependence of the linear expansion coefficient turns out to be that of the specific heat, that is $\approx a.T + b.T^3$, being the first term the electronic contribution and the second one the phonon contribution. As a consequence, at low temperatures the thermal expansion coefficient α deviates from linearity (see for example Fig. 2.5a in [34]) and in fact it goes to zero slope as temperature approaches absolute zero.

Actually, the observed plateau in the range from 5 to some 70–80 K could be considered, at a sight, a trend of the appearance of the Invar effect. Invar and anti-Invar effects are governed by electronic properties and related to anharmonic enhacement of the total energy in the ground state. In the case of FeCo alloys, that anharmonicity is caused by the simultaneous presence of states with different magnetic character (ferromagnetism and antiferromagnetism or spin disorder), and associated to the simultaneous presence, with different percentages, of
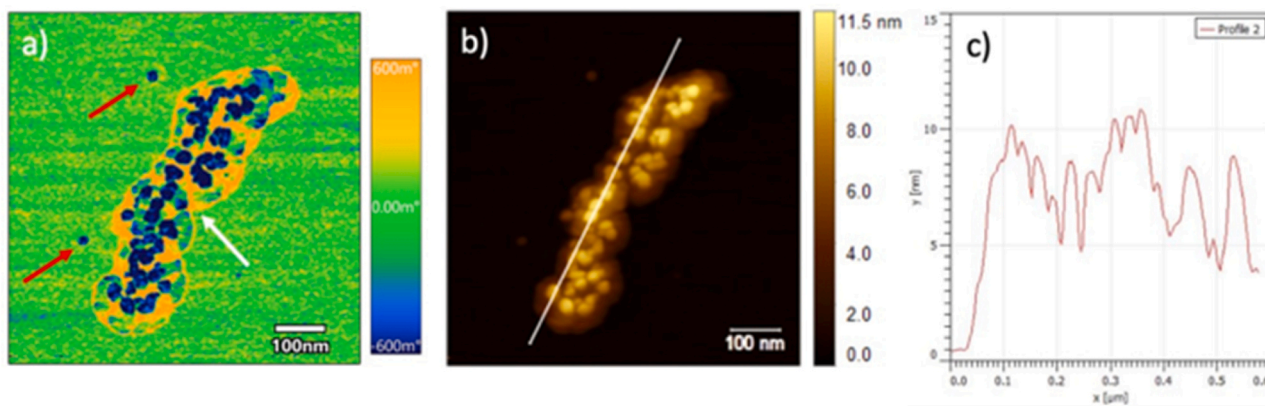
Fig. 3. a) MFM phase shift image for the FeCo composition nanoparticles, showing both single nanoparticles (red arrows) and one agglomerate of them (white arrow); b) its corresponding topographical image; c) nanoparticles agglomerate profile along the white line marked in b).
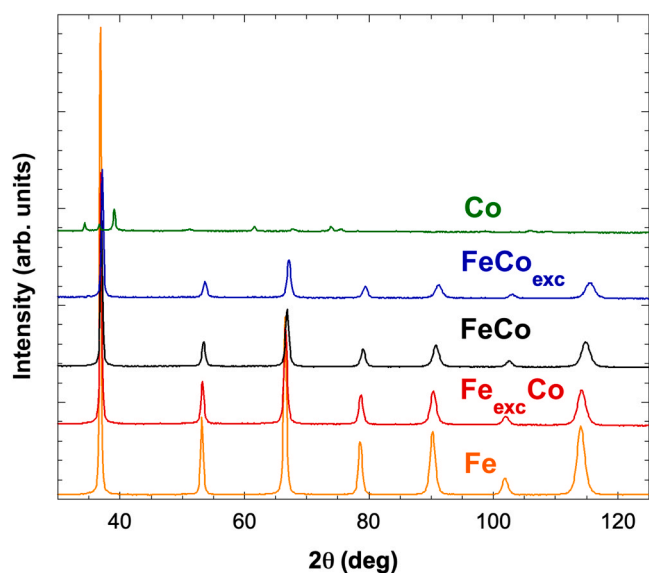

Fig. 4. Room temperature ND patterns of the raw powder of Fe, Co and FeCo alloys.

unique crystallographic structure (cubic bcc) for the three studied FeCo different composition alloys. On the other hand and as it will be further discussed, room temperature Mössbauer spectra show undoubtedly one magnetic state for Fe leading to nice fits by using an only broad sextet.

Moreover, well established Invar alloys like $Fe_{64}Ni_{36}$, exhibit a very low thermal expansion coefficient α below 2×10^{-6} K^{-1} around room temperature compared to most metallic materials which have α values about $10–20 \times 10^{-6}$ K^{-1} [36]. The synthesized Fe and FeCo NPs show thermal expansion coefficient values much more close to that of common metallic materials.

The procedure to extract the structural EXAFS signal ($k \bullet \chi(k)$) followed the standard steps of pre-edge background removal followed by a spline modeling of bare atomic background, edge step normalization through a polynomial function interpolated far above the edge region and energy calibration using the software ATHENA [37,38]. The modelling of atomic clusters centered on the absorber atom was obtained by ATOMS using atomic coordinates from Crystallographic Information Files (CIFs) [39]. Theoretical amplitude and phase functions were generated using the FEFF6 code [40]. Finally, EXAFS spectra were fitted through the ARTEMIS software [38] in the Fourier-Transform (FT) space; the analysis have been extended to the range of $1.5 – 5.7$ Å for all the samples, showing signals from further coordination shells.

Fig. 6 shows the XAS spectra in the XANES region of $FeCo_{exc}$ (lowest Fe/Co ratio) $Fe_{exc}Co$ (highest Fe/Co ratio) nanoparticles at the Co and Fe K-edges (Fig. 6a and b, respectively), each one compared with the two pure Co and Fe nanoparticle samples (Fe NPs and Co NPs) and Fe- and Co-based standard compounds (Fe and Co pure elements foils as
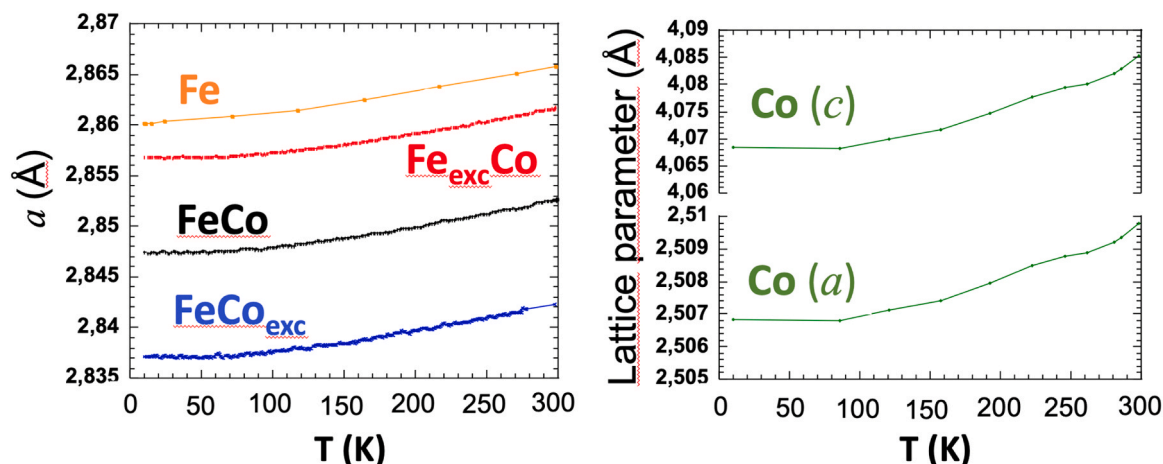
different crystallographic structures, cubic bcc and fcc (extensive information can be found in [35]). This is not the case of our synthesized FeCo NPs: on the one hand, neutron diffraction patterns have shown a

Fig. 5. Variation of the lattice parameters obtained from NPD patterns with the temperature of the raw powders of Fe, Co and FeCo alloys.
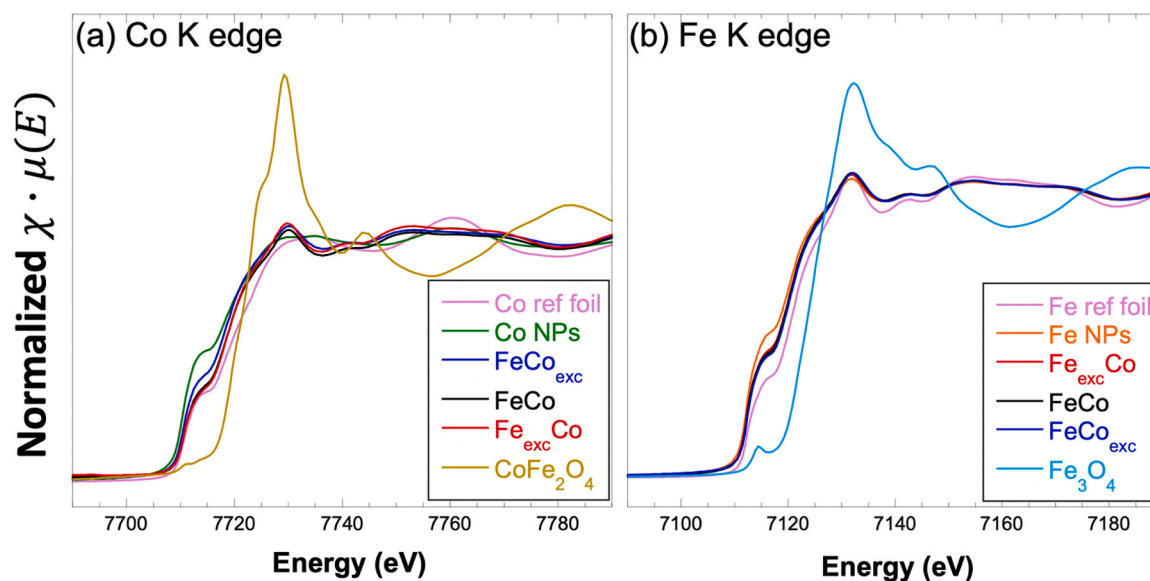
Fig. 6. Normalized XANES spectra of (a) Fe_xCo_{100-x} alloys, Co NPs and related standards at the Co K edge, and (b) Fe_xCo_{100-x} alloys, Fe NPs and related standards at the Fe K edge.

references and oxides like Fe_3O_4, $CoFe_2O_4$ and Co_3O_4). The Co absorption edge values for $FeCo_{exc}$, the metallic foil (Co foil) and the pure Co NPs are identical (7709 eV) while the shape of the XANES spectra are similar only for Co foil and Co NPs because of the hcp structure shared between them ($FeCo_{exc}$ presents a bcc structure instead, see EXAFS analysis in the following), even if a marked shift in the normalized intensity points out the inability of describing the nanoparticle sample as bulk-based material. Another difference is the lower amplitude of the oscillations above the edge, which is also typical of a nanostructured material [41]. The higher is the oxidation state of the studied element the higher is the energy of its edge position as well, so as the presence of pre-edge features which is distinctive for non-centrosymmetric sites. These characteristics can be seen in the $CoFe_2O_4$. For the $FeCo_{exc}$ alloy, the similarities with the Co foil spectrum, the position of the edge and the absence of pre-peak features indicate that Co is in the metallic state, without detectable amounts of Co oxides. Similar behavior is observed for FeCo and $Fe_{exc}Co$ nanoparticles, which only exhibit a slight decrease in the normalized intensities proportional to the decrease of Co content.

A clearer trend is depicted for the Fe samples at the Fe K edge, due to the same bcc structure shared among Fe_xCo_{100-x} alloys, Fe NPs and Fe foil. These samples present the same edge value (7712.3 eV), noticeably lower than the Fe 2+/3+-based standards, as well as similar overall XANES trends, with differences in the normalized intensities and absence of pre-edge peaks. No evidence of Fe-oxides presence has been detected all over the Fe_xCo_{100-x} samples or in the Fe NPs.

Structural refinement of the Fe and Co local environments (up to 5–6 Å from the absorber atom) was performed by least square minimization of the EXAFS signals (from ~150 eV above the absorption edge) of the Fe, Co and Fe_xCo_{100-x} alloy nanoparticle samples (see Figs. 7 and 8). A full description of the refinement procedure can be found in the Supplementary Material (S2 in SM). After using ATOMS to generate a list of all the atomic coordinates in a cluster of 6 Å size and the FEFF6 software to calculate all the photo-electron scattering functions, the resulting paths were manually selected in order to obtain the best possible fits. Particular attention was given to the first five Fe-Fe and Co-Co single backscattering paths used as reference parameters for refining the Fe-Fe and Co-Co distances.

The Fe NPs and Co NPs EXAFS analysis highlighted an excellent agreement between the crystallographic distances of the starting CIF files and the found ones (see Fig. 7 and Table 2). The Co NPs local structure is perfectly described by the standard hexagonal hcp Co lattice,

with only a 0.01 Å first shell contraction between experimental data and CIF model, both in-plane and out-of-plane (that is in path 1 and 2, see S3.1 in SM) while the Fe NPs spectrum matches the standard cubic α-bcc iron lattice, with a more pronounced average contraction of 0.02 Å all over the investigated shells (see Table 2). This light contraction can arise from the difference of temperature between the used CIF data, acquired at 298 K, and the samples data temperature acquired at 10 K. These results confirm the XANES findings (see Fig. 6) in terms of absence of Fe-O and Co-O signals and good structure correspondence between CIF models and our alloy samples spectra.

Regarding the FeCo alloys, similar conclusions can be drawn, independently from the Fe/Co ratio, such as the absence of Fe- and Co-oxides evidences and a good correspondence with the crystallographic model used. The reference model resulting from all the best fits is exclusively the bcc, both at the Fe and the Co K edges, since the hcp Co turns out to be not suitable for describing any of the above samples, in particular the considerable splitting of the first shell distances. The use of a Fe-based standard to fit Co K edge signals is appropriate due to the close similarity between the Fe and Co photoionization cross-sections [42], while the adoption of a bcc crystal model attests the interchangeability of the two metals inside the FeCo alloy structure, since there is no evidence of relevant Co hcp structure presence. Despite the low-temperature measurements, it was not possible to discriminate between Co-Co, Co-Fe and Fe-Fe signals due to the close similarity between the photoelectron backscattering functions and typical bond distances of the two elements. The Fe and Co local structures, studied at the Fe and Co K edges respectively, match with good agreement the α-bcc iron CIF, with bond lengths values which approach the Fe NPs sample as the Fe/Co increases (see Fig. 8, Table 3 and Table 4). The multiple-edge fits, where the two edges are used simultaneously, lead to the same results (see Table 5).

Again, the observed slight contraction between bcc Fe and our samples bond lengths can be explained from the difference of temperature between the used CIF data, acquired at 298 K, and the samples data acquired at 10 K. Regarding the S_0^2 value, which describes the amplitude of the EXAFS signal a considerable reduction is reported (Co foil: $S_0^2 = 0.79$ +/- 0.03 fitted with hcp Co CIF; Fe foil: $S_0^2 = 0.80$ +/- 0.06 fitted with bcc Fe CIF) that would point to a reduced dimensionality of the particles [41,43,44]. However, and applying the data for bcc Fe published by Beale & Weckhuysen [45], it would correspond to particles of 1–2 nm of diameter, a size that is not in agreement with our previous microscopy observations. Considering that the fits could include also the
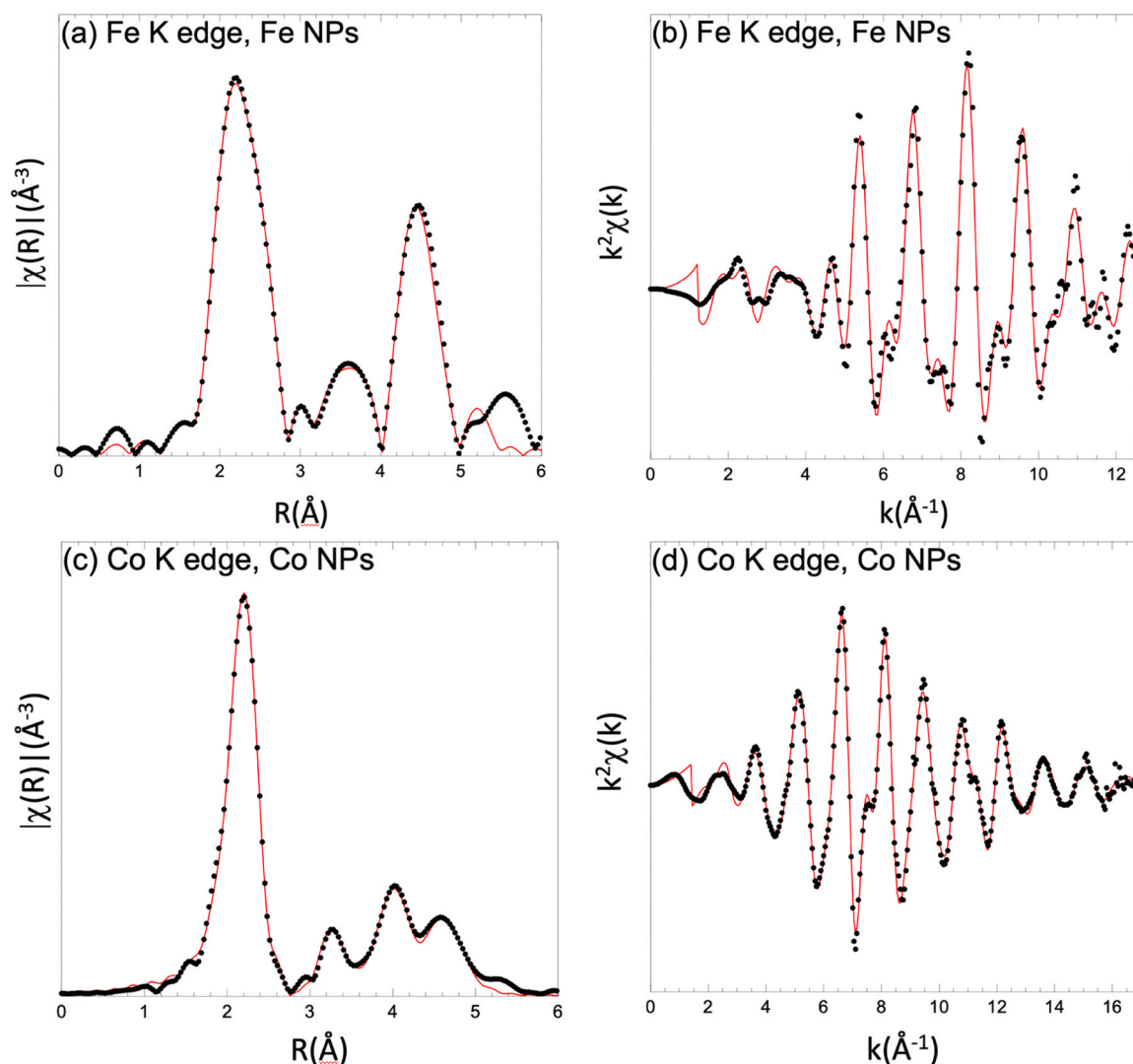
Fig. 7. Fourier transform module (transformation window in the range $k = 2$–11.6 Å^{-1} for the Fe K edge spectrum and $k = 2$–15.6 Å^{-1} for the Co K edge one) of the EXAFS spectra for the Fe NPs (a) and Co NPs (c) samples, analysed at the Fe and Co K edges respectively, together with the correspondent k-space signals ((b) and (d) respectively) (k^2-weighted). Black dots are experimental data, solid red lines are the best obtained fit.

higher coordination shells (that would be strongly depleted in case of reduced size), we conclude that the amplitude parameters cannot be exploited for an estimation of the particle size. Thus, the FeCo alloy nanoparticles appear homogeneous despite the Fe/Co ratio, without apparent nano-segregation of different phases.

A clear trend validated by the three different fit approaches (see Fig. S3.2 in SM) seems to point to a slight increase of the bond lengths all over the five paths considered, which is directly proportional to the Fe content (0.013 and 0.026 Å for path 1 and path 10 respectively for the ≈ 30 % increase in Fe content from the FeCo$_{exc}$ composition to the Fe$_{exc}$Co one). Finally, calculated Fe$_x$Co$_{1-x}$ alloys nanoparticles compositions from the ratio of the normalized edge steps at the Fe and Co edges can be seen in Table 6. It can be observed that compositions calculated from EXAFS measurements are slightly different than those obtained from ICP analysis and more similar to the expected ones from the stoichiometry of the precursors. This discrepancy is more related to the treatment of the sample before the analysis than to the technique itself. EXAFS measurements have been performed directly in the NPs powders, so the relation between the normalized edge steps is proportional to the Fe/Co content in the sample. Nevertheless, when performing ICP analysis, it could happen that solution of both metals was not very efficient and that small amounts of metals were left undissolved. This could be the reason

of the discrepancies in ICP for the samples. Similar discrepancies have been also observed in other FeCo alloy nanoparticles synthesized by chemical methods [46,47].

Fig. 9 shows the room temperature hysteresis loop measured for the Fe, Co and Fe$_x$Co$_{100-x}$ nanoparticles (hysteresis loops measured at 5 K can be found in Fig. S4.1 of the SM). Table 6 summarizes the different magnetic characteristics obtained for each sample.

In all samples magnetic saturation is clearly observed at applied magnetic field values above 2 MA/m (or above 2.5 T). The measured values of the room temperature saturation magnetization of our synthesized Fe and Co NPs well agree (within the experimental error) with the accepted values in the bulk state for pure Fe and Co, that is M$_S$ = 221.9 Am^2/kg and 162.5 Am^2/kg at R.T., respectively [48]. For the Fe$_x$Co$_{100-x}$ alloys, measured saturation magnetization follows previously well-known observations (see for example Figure 4.21(b) in [48]): the addition of cobalt increases the magnetization of the FeCo alloy, and the 30 % cobalt-content composition has the highest measured M$_S$ value at room temperature than any other known material.

All our measured hysteresis curves show also low coercive field values, confirming the soft magnetic character of all the synthesized nanopowders. As expected, the anisotropic character of pure Co reflects in a higher coercivity (about 17 kA/m at room temperature) than the
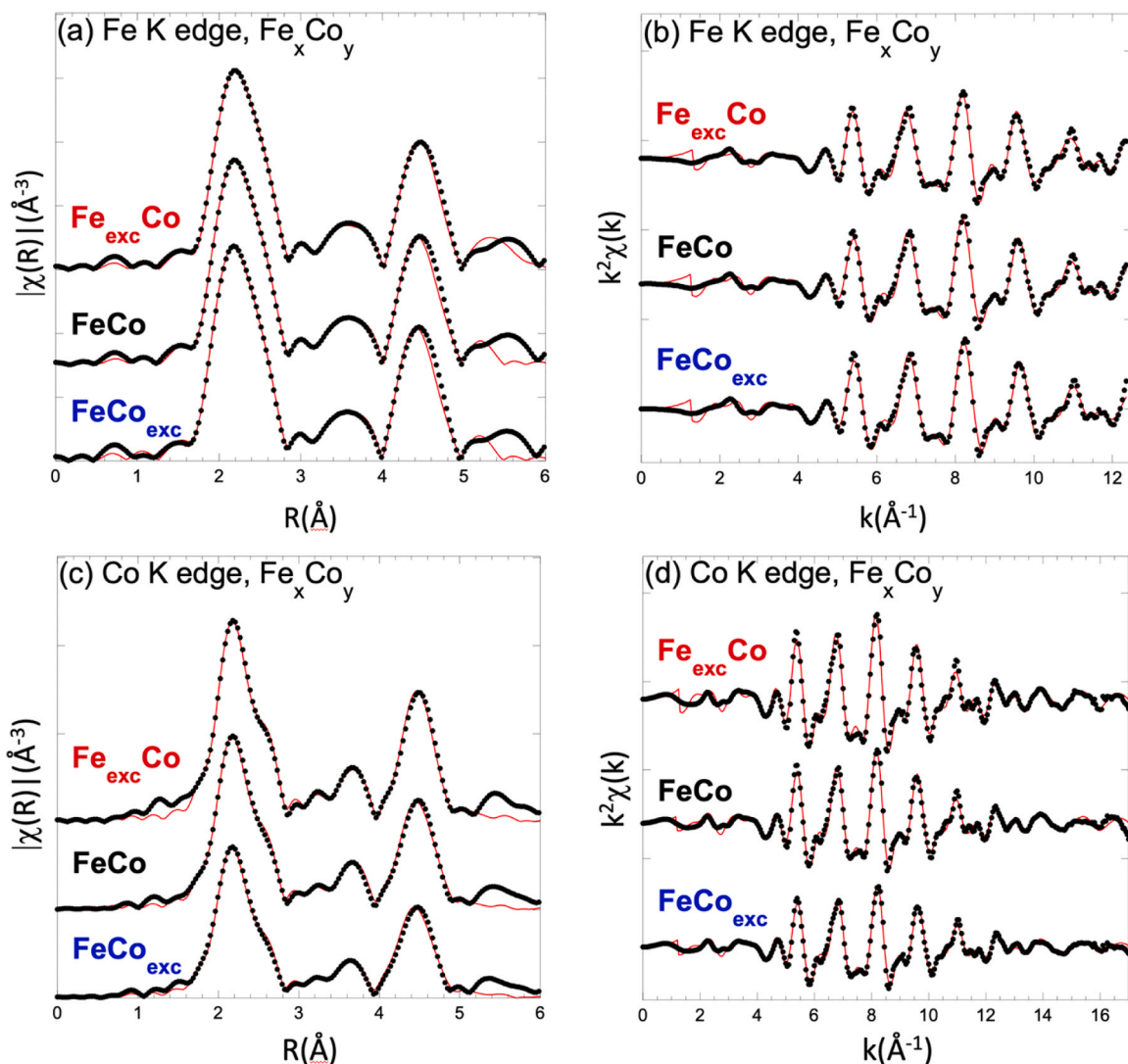
Fig. 8. Fourier transform module (transformation window in the range $k = 2$–11.6 Å^{-1} for Fe K edge spectra and $k = 2$–15.6 Å^{-1} for Co K edge ones) of the EXAFS spectra for the three Fe$_x$Co$_{100-x}$ alloy samples, analysed at the Fe (a) and Co K edge (c), together with the correspondent k-space signals ((b) and (d) respectively) (k^2-weighted). Black dots are experimental data, solid red lines are the best fit. All the spectra are shifted vertically for better visualization.

Table 2
structural parameters of the best fits from Fig. 7 obtained by multiple-shell fitting of the Fe NPs and Co NPs EXAFS spectra using Fe bcc and Co hcp base models respectively (see Supplementary Material).

Fe and Co nanoparticles						
Sample		Path 1	Path 2	Path 5	Path 8	Path 10
Fe NPs	S_0^2	$0.42 \pm 0,06$				
	$R(\text{Å})$	2.465 ± 0.007	2.84 ± 0.01	4.037 ± 0.008	4.733 ± 0.009	4.944 ± 0.01
	$\sigma^2(\text{Å}^2)$	0.0028 ± 0.0012	0.0029 ± 0.0029	0.0049 ± 0.0012	0.0048 ± 0.0012	0.0047 ± 0.0029
Sample		Path 1	Path 2	Path 3	Path 7	Path 10
Co NPs	S_0^2	0.39 ± 0.01				
	$R(\text{Å})$	2.486 ± 0.002	2.497 ± 0.002	3.539 ± 0.003	4.069 ± 0.004	4.337 ± 0.004
	$\sigma^2(\text{Å}^2)$	0.0042 ± 0.0002	0.0042 ± 0.0002	0.0066 ± 0.0002	0.0065 ± 0.0002	0.0065 ± 0.0002

pure Fe one (only 2 kA/m). For the Fe$_x$Co$_{1-x}$ alloy nanoparticles, this room temperature coercivity ranges between 4.8 and 5.7 kA/m, close to the desired good soft magnetic behavior [49]. At low temperature, 5 K, we have measured a slightly increase both in the saturation magnetization value as well as the coercive field for all samples, but the soft magnetic character observed at room temperature remains. Close attention should be payed to the remanence-to-saturation (M_r / M_S)

magnetization value at R.T., of the order of 10^{-2} in all the studied alloys. This fact will be subject of further discussion.

In Fe$_x$Co$_{100-x}$ alloys, the measured saturation magnetization values clearly correlate with the atomic order and level mixing of Fe and Co atoms and subsequent redistribution of spin states in the Fe sites. This fact arises from the dependence of the Fe and Co magnetic moment values on their environment: while magnetic moment of Co atoms does

Table 3

Structural parameters of the best fits from Fig. 8a and b obtained by multiple-shell fitting of the Fe_xCo_{100-x} alloys EXAFS signals acquired at the Fe K edge, employing Fe bcc as base model.

Fe_xCo_y alloy nanoparticles (Fe K edge)						
Sample		Path 1	Path 2	Path 5	Path 8	Path 10
$FeCo_{excess}$	S_0^2	0,55 ± 0,08				
	$R(Å)$	2.455 ± 0.006	2.83 ± 0.01	4.021 ± 0.008	4.715 ± 0.009	4.924 ± 0.01
	$\sigma^2(Å^2)$	0.0035±0.0011	0.0043±0.0015	0.0058±0.0011	0.0057±0.0011	0.0056±0.00215
FeCo	S_0^2	0.53 ± 0.08				
	$R(Å)$	2.465 ± 0.006	2.834 ± 0.01	4.035 ± 0.008	4.731 ± 0.009	4.94 ± 0.01
	$\sigma^2(Å^2)$	0.0036±0.0011	0.0042±0.0014	0.0058±0.0012	0.0056±0.0014	0.0056±0.0012
$Fe_{excess}Co$	S_0^2	0.46 ±0.05				
	$R(Å)$	2.470 ±0.005	2.847 ± 0.009	4.044 ± 0.008	4.74 ± 0.010	4.95 ± 0.010
	$\sigma^2(Å^2)$	0.0026±0.0012	0.003± 0.0012	0.0053±0.0012	0.005 ±0.0012	0.0051±0.0012

Table 4

Structural parameters of the best fits from Fig. 8c and d obtained by multiple-shell fitting of the Fe_xCo_{100-x} alloys EXAFS signals acquired at the Co K edge, employing Fe bcc as base model.

Fe_xCo_y alloy nanoparticles (Co K edge)						
Sample		Path 1	Path 2	Path 5	Path 8	Path 10
$FeCo_{excess}$	S_0^2	0,48 ± 0,03				
	$R(Å)$	2.459 ± 0.003	2.832 ± 0.006	4.022 ± 0.004	4.716 ± 0.005	4.925 ± 0.005
	$\sigma^2(Å^2)$	0.0031±0.0004	0.0046±0.0008	0.0059±0.0004	0.0057± 0.0006	0.0057± 0.0004
FeCo	S_0^2	0.56 ± 0.03				
	$R(Å)$	2.463 ± 0.003	2.840 ± 0.005	4.033 ± 0.004	4.729 ± 0.005	4.939 ± 0.005
	$\sigma^2(Å^2)$	0.0033±0.0004	0.0042±0.0007	0.0055±0.0004	0.0053±0.0007	0.0053±0.0004
$Fe_{excess}Co$	S_0^2	0.63 ± 0.04				
	$R(Å)$	2.468 ± 0.003	2.853 ± 0.005	4.040 ± 0.004	4.738 ± 0.005	4.948 ± 0.005
	$\sigma^2(Å^2)$	0.0032±0.0004	0.0040±0.0007	0.0052±0.0004	0.0051±0.0004	0.0051±0.0007

Table 5

Structural parameters obtained by multiple-shell fitting using concurrently both of the Fe_xCo_{100-x} alloy EXAFS signals acquired at the Fe and Co K edge, employing Fe bcc as base model.

Fe_xCo_y alloy nanoparticles (Fe and Co K edges)						
Sample		Path 1	Path 2	Path 5	Path 8	Path 10
$FeCo_{excess}$	S_0^2 (Fe K)	0.53 ± 0.03				
	S_0^2 (Co K)	0.48 ± 0.03				
	$R(Å)$	2.455 ± 0.003	2.830 ± 0.004	4.021 ± 0.004	4.715 ± 0.005	4.925 ± 0.005
	$\sigma^2(Å^2)$	0.0032±0.0004	0.0043±0.0006	0.0060±0.0004	0.0058±0.0005	0.0058±0.0005
FeCo	S_0^2 (Fe K)	0.53 ± 0.03				
	S_0^2 (Co K)	0.57 ± 0.03				
	$R(Å)$	2.465 ± 0.003	2.839 ± 0.004	4.036 ± 0.004	4.733 ± 0.005	4.943 ± 0.005
	$\sigma^2(Å^2)$	0.0034±0.0004	0.0043±0.0006	0.0056±.0005	0.0055±.0004	0.0055±.0005
$Fe_{excess}Co$	S_0^2 (Fe K)	0.47 ± 0.03				
	S_0^2 (Co K)	0.63 ± 0.04				
	$R(Å)$	2.469 ± 0.003	2.848 ± 0.004	4.042 ± 0.004	4.740 ± 0.005	4.951 ± 0.005
	$\sigma^2(Å^2)$	0.0029±0.0004	0.0037±0.0006	0.0052±.0004	0.0050±.0005	0.0050±.0006

Table 6

Magnetic properties obtained for Fe, Co and Fe_xCo_{100-x} alloys NPs.

Sample composition (ICP)	Sample composition (EXAFS)	M_S (Am^2/kg)[*1]		H_c (kA/m)[*2]		M_r / M_S	
		5 K	300 K	5 K	300 K	5 K	300 K
Fe	Fe	224.6	220	3	2	0.008	0.012
$Fe_{66}Co_{34}$	$Fe_{74}Co_{26}$	232.5	228.3	8	4.8	0.038	0.023
$Fe_{51}Co_{49}$	$Fe_{62}Co_{38}$	224.3	220	10	5.7	0.034	0.022
$Fe_{33}Co_{67}$	$Fe_{45}Co_{55}$	213.6	210.7	8.8	5.4	0.036	0.023
Co	Co	161.2	158.2	31.8	17	0.101	0.070

[*1] Error in magnetization measurement: 0.5 % of measured value.
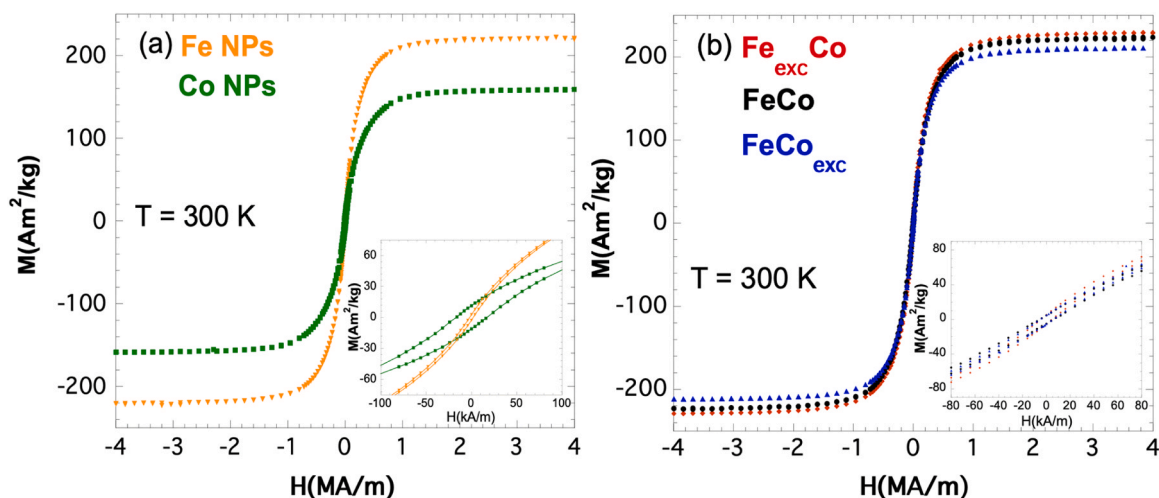[*2] Error in magnetic field determination: ±1 kA/m.

Fig. 9. Room temperature hysteresis loops of the a) pure Fe and Co NPs and b) Fe_xCo_{1-x} NPs. Inset shows an amplified zone of each hysteresis loop in order to observe the coercive field values.

not show any change, that of Fe actually does, increasing from 2.2 μ_B in pure Fe to about 3 μ_B in full ordered equiatomic FeCo [7]. Owing to its sensitivity to local chemical and structural alterations in the vicinity of iron (Fe) atoms, Mössbauer spectroscopy serves as a valuable technique for probing atomic disorder. Fig. 10 shows the ^{57}Fe Mössbauer spectrum corresponding to synthesized pure Fe and Fe_xCo_{100-x} NPs samples.

All the spectra are characterized for presenting an only broad sextet with decreasing average hyperfine field as the Co content of the sample increases. Notably, there are no discernible additional components at

Fig. 10. Room temperature Mössbauer spectra of the pure Fe and Fe_xCo_{100-x} NPs studied in this work.

higher velocities or the characteristic 33 T signal associated with bcc-Fe. This observation unequivocally indicates that all the iron (Fe) atoms are incorporated within the Fe_xCo_{1-x} alloy, with no presence of iron oxides or clusters of bcc-Fe.

The nearly symmetrical nature of the spectra signifies that the Fe atoms are located in highly symmetric crystallographic positions, providing confirmation of a cubic structural arrangement surrounding the Fe atoms in the alloys, as previously stated by NPD and EXAFS and XANES techniques.

The influence of an impurity or atomic substituent in the neighborhood of the Fe in Fe based alloys on the hyperfine parameters has been profusely studied [50–52]. The hyperfine field and isomer shift exhibit remarkable sensitivity to the quantity and nature of atomic substitutions, yielding each distinct local environment around the Fe atom a unique Mössbauer component. The relative resonant area of each constituent within the overall spectrum depends on the stoichiometry and arrangement of these substituents and can be estimated using a binomial distribution approach [50,51].

Nonetheless, when dealing with Fe-Co alloys, the close chemical and magnetic resemblance between Fe and Co often results in subtle differences among the spectral components associated with neighborhoods featured by a continuous range of Co atoms. In cases where the number of potential spectral components is relatively high, it becomes challenging to make meaningful and univocal comparisons among the components of the spectra obtained from alloys with different Co content.

We have qualitatively evaluated the spectra, fitting them by means of a hyperfine field distribution and we have established a lineal correlation between the isomer shift and hyperfine field values. In Fig. 11, we present the normalized hyperfine field distributions $<B_{hf}(T)>$ obtained from the synthesized Fe_xCo_{100-x} samples under study. The hyperfine parameters resulting from the fitting process appear summarized in Table 7.

As it can be observed, the hyperfine field distribution for the FeCo sample, centered at approximately 34.7 T, exhibits a notably broader profile compared to those of the $Fe_{exc}Co$ and $FeCo_{exc}$ samples with higher (36.3 T) and lower (33.9 T) average hyperfine field values, respectively.

Depending on, among others, the processing and composition, Fe-Co alloys can present A2 disordered solid solution or B2 ordered body center cubic arrangements. In an equiatomic ordered Fe-Co alloy with a B2 ordering, Fe atoms exclusively occupy the center of the cubic structure, surrounded by eight corner-located Co atoms. These atoms arrangement results in only one non-equivalent Fe atom within the
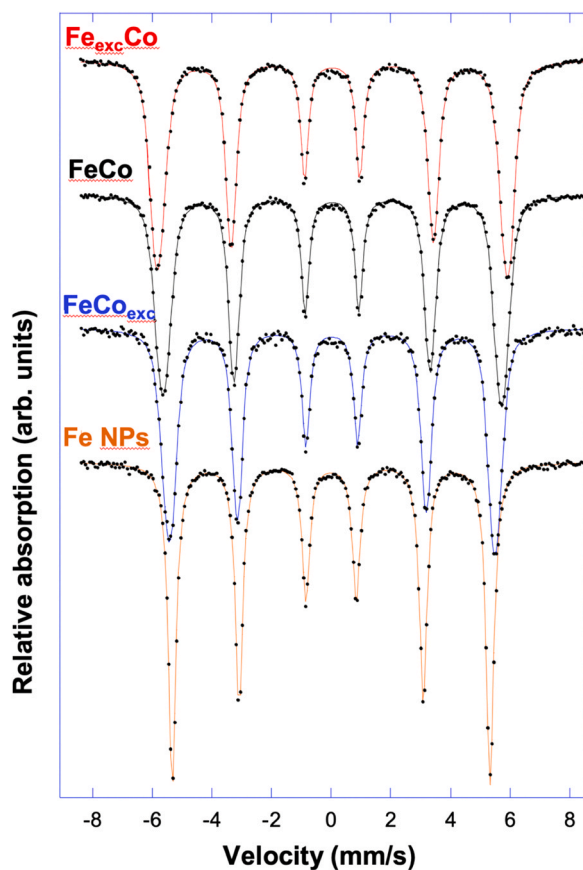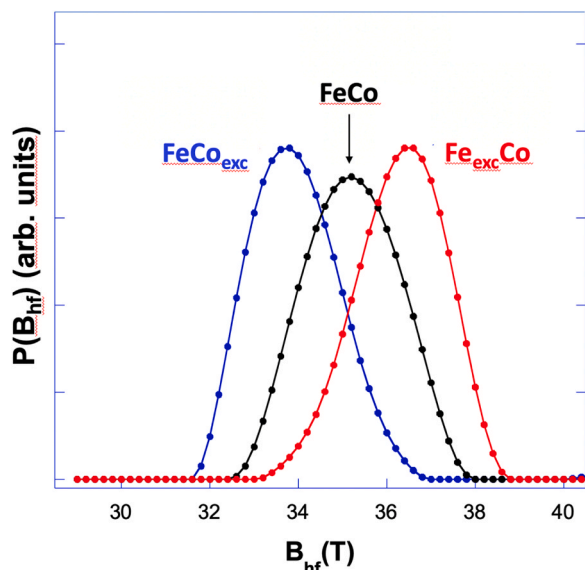
Fig. 11. Room temperature hyperfine field distribution obtained from Mössbauer spectra of the Fe_xCo_{1-x} NPs studied in this work.

Table 7

Room temperature hyperfine parameters obtained from Mössbauer spectra fit (IS: isomer shift; QS: quadrupole splitting; $<B_{hf}$ (T)$>$: magnetic field distribution main value; $B_{hf\ max}$ (T): maximum field value of the distribution). Value of room temperature saturation magnetization obtained by SQUID magnetometry also appears for trend comparison purpose.

Sample	IS (mm/s)	QS (mm/s)	$<B_{hf}$ (T)$>$	$B_{hf\ max}$ (T)	M_S (Am²/kg) (300 K)
Fe	0.00	0.00	–	33.0	220
Fe_{exc} Co	0.04	0.00	36.3	36.4	228.3
FeCo	0.04	0.01	35.2	34.7	220
$FeCo_{exc}$	0.03	0.01	33.9	33.8	210.7

structure, which in turn generates a uniquely defined Mössbauer spectrum.

In a solid solution structure where Co and Fe atoms are randomly distributed, the number of non-equivalent Fe atoms is primarily determined by their varying local environments. These local environments are defined by the number of Co atoms in proximity to each Fe atom, resulting in distinct Mössbauer components. Since the relative resonant area of each spectral component is determined by a binomial distribution, the Mössbauer spectrum of an equiatomic disordered Fe-Co alloy would exhibit a greater number of significant components. In contrast to the B2-structured alloy, this spectrum would be considerably broader when compared to the spectra of Fe-Co alloys with different compositions. Furthermore, in alloys featuring a relatively high Co content ($x \leq 0.5$), notable distinctions of up to 1 Tesla have been observed between the hyperfine fields of the ordered and disordered phases. It is noteworthy that the average hyperfine values observed in our examination of the Fe_xCo_{1-x} samples align with those previously reported for the same compositions within the disordered configuration [53,54].

To sum up, Mössbauer spectroscopy provides compelling further evidence that the chemically synthesized Fe_xCo_{100-x} samples under study exist in an A2 type disordered solid solution, with compositions close to the nominal values obtained through inductively coupled plasma analysis (ICP). The obtained Fe_xCo_{1-x} alloy nanoparticles show high purity and small and "flaky" shape, with a higher amount of Fe than the initially expected one, very high magnetization very close to that of the bulk compositions accompanied by good soft magnetic properties and long-time stability in air.

The last task to be discussed concerns the unusual high values

previously observed for the anisotropy of our synthesized FeCo alloy nanoparticles, in the range of MJ/m³. The reported value of magnetocrystalline anisotropy for $Fe_{50}Co_{50}$ alloy is about 15–20 kJ/m³ [16]. However, previous work from Ibrahim *et al.* [55] reported an anisotropy value of 0.38 MJ/m³ in equiatomic $Fe_{50}Co_{50}$ superparamagnetic small nanoparticles (6 nm size). Also, the change of the initially determined α-bcc cubic to a slightly distorted ($c/a > 1.05$) bct tetragonal structure has been proven to be in the origin of anisotropy values of some MJ/m³ in these FeCo alloys (see, for example, [56,57]). In fact, calculations made by Burkert *et al.* [58] point towards a maximum anisotropy value for the distorted bct structure for FeCo alloys of about 10 MJ/m³.

In the previous work from the own authors (with the same FeCo alloy nanoparticles) values of the effective anisotropy constant K_{eff} as high as 1.8–2 MJ/m³ were determined [15]. This estimation of K_{eff} by using the law of approach to saturation (LAS, $M/M_S \approx 1-b/H^2$) [59,60] was made on the basis of the bcc cubic symmetry observed by X-ray diffraction measurements, with no knowledge about synthesized NPs morphology.

Hence, the relationship $b = \left(\frac{8}{105}\right)\left(\frac{K_{eff}}{\mu_0 M_S}\right)^2$ [60] was used to determine such K_{eff} value. Those obtained values can be considered as a first approximation to the true anisotropy values of our synthesized FeCo NPs.

The evidences obtained from the different techniques and measurements presented in this work will help to understand the origin of that high anisotropy value. To start, NPD and EXAFS and XANES techniques have clearly stated that the synthesized Fe_xCo_{1-x} alloys show a single α-bcc cubic structure (as the pure Fe nanoparticles also synthesized do) with no presence of Fe- or Co-oxides as impurities. No trace of distorted bct tetragonal structure has been observed. But more important, only AFM/MFM technique has revealed an unexpected "flaky" morphology for the NPs. That is, the law of approach to saturation has to be applied by considering the case of particles with strong uniaxial anisotropy.

Now, the value $b = \left(\frac{4}{15}\right)\left(\frac{K'_{eff}}{\mu_0 M_S}\right)^2$ [61] has to be used and therefore obtained values of effective anisotropy K'_{eff} have been re-calculated and are in the range 0.98–1.11 MJ/m³, lower than the previously obtained ones but, in any case, of the same order of magnitude (MJ/m³).

Most of the existing models found in the literature assume that magnetic nanoparticles have an intrinsic uniaxial anisotropy independently if they are considered as isolated entities or as part of bigger agglomerates. When purity of the composition is guaranteed (as it is in our case), the main contributions to that total effective value K_{eff} will be just the magnetocrystalline (K_{mag}, that mainly depends on the morphology and chemical composition of the material) and shape anisotropy (K_{sh}, that essentially reflects how much the shape of the nanoparticle is deviating from a perfect sphere) ones (see for example [57,62]). Shape is an attribute of the particle as an object, not of the FeCo alloy itself. With very high magnetization in such an asymmetric particle, magnetic anisotropy of shape will also be very high. Shape anisotropy (K_{sh}) can be independently estimated from AFM/MFM and TEM observations and compared with the vales of K_{eff} previously obtained: we can assume each of our flake-shaped nanoparticle to have the geometry of an oblate spheroid with $a < b = c$ (see Fig. 12). Each of these nanoparticles behaves as a small magnet generating an external magnetic field, but also a "demagnetizing field H_d" within the particle that opposes the external one and turns out to be proportional to the particle own magnetization: $H_d = -N.M$, where N is the so called "demagnetizing factor" along each of the main directions of the corresponding geometrical shape.

In the case of an oblate spheroid-like geometry [40],

$$N_b = N_c = \frac{1}{2(m^2-1)}\left[\frac{m^2}{\sqrt{m^2-1}}\sin^{-1}\left(\frac{\sqrt{m^2-1}}{m}\right)-1\right]$$
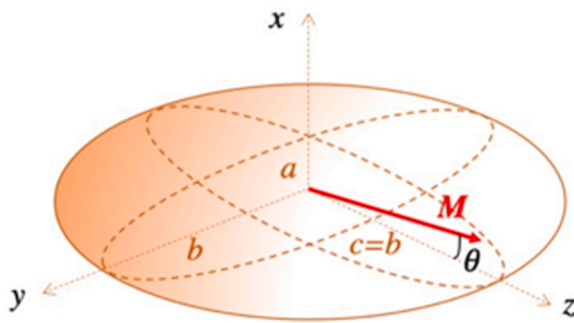
$$N_a = 1 - 2N_c$$

Fig. 12. Graphic representation of an Fe_xCo_{1-x} alloy single nanoparticle as an oblate spheroid, with its magnetization M lying in the xz plane.

with the aspect ratio $c/a = m$. As this value increases, the demagnetization factor along the c axis decreases while the one in the a direction increases. As a first consequence, spin arrangements along that c direction are energetically more favorable than in the a direction, and so magnetization is energetically more stable and remains in the plane of our flake-shaped nanoparticles. Thus, we can now evaluate the shape anisotropy energy E_{sh} that will affect any magnetization process:

$$E_{sh} = \frac{1}{2}\mu_0 \overrightarrow{M} D \overrightarrow{M} = \frac{1}{2}\mu_0 M^2 \begin{pmatrix} \sin\theta \\ 0 \\ \cos\theta \end{pmatrix} \begin{pmatrix} N_a & 0 & 0 \\ 0 & N_b & 0 \\ 0 & 0 & N_c \end{pmatrix} \begin{pmatrix} \sin\theta \\ 0 \\ \cos\theta \end{pmatrix}$$

$$\approx \frac{1}{2}\mu_0 M^2 N_a \sin^2\theta$$

being D the demagnetizing tensor matrix and $K_{sh} = \frac{1}{2}\mu_0 M^2 N_a$ the value of the shape-anisotropy constant. For the $FeCo_{exc}$ alloy nanoparticle and assuming its shape as appearing in Fig. 12, considering $a \approx 2$ nm, $b = c \approx 24$ nm it can be calculated that $N_b = N_c = 0.03846$ and $N_a = 0.923$. Therefore, a single nanoparticle exhibits an anisotropy constant value about $K_{sh} \approx 1.76$ MJ/m^3. Table 8 shows the K_{sh} values obtained for the three Fe_xCo_{1-x} alloys of our study, considering the same previous size of a small nanoparticle.

Finally, and as previously stated, our Fe_xCo_{1-x} alloys show a very low remanence-to-saturation (M_r / M_S) magnetization room temperature value (see values at Table 6). The intensity of the magnetic dipolar interaction among nanoparticles is in the origin of this observation [63]. Two magnetic dipoles $\overrightarrow{m_1}$ and $\overrightarrow{m_2}$ separated by a distance $\overrightarrow{r}$ have an interaction energy density equal to [64]

$$E_{d-d} = \frac{\mu_0}{4\pi r^3}\left[\overrightarrow{m_1} \bullet \overrightarrow{m_2} - \frac{3}{r^2}(\overrightarrow{m_1} \bullet \overrightarrow{r})(\overrightarrow{m_2} \bullet \overrightarrow{r})\right]$$

that depends not only on the distance between them but also on their mutual alignment. Let us consider, using the same particle geometry as in Fig. 12, the nanoparticles and magnetic moments disposition that is represented in Fig. 13. This figure shows the FeCo nanoparticles

Table 8
K_{sh} values obtained for the three FeCo alloys of our study, and considering the size of an observed small nanoparticle ($a \approx 2$ nm, $b = c \approx 24$ nm). Values of K'_{eff} obtained by using the law of approach to saturation and estimated with the same nanoparticles also appear for comparison.

Sample composition (ICP)	Sample composition (EXAFS)	K'_{eff} (MJ/m^3)	M_S (A/m)	K_{sh} (MJ/m^3)
$Fe_{66}Co_{34}$	$Fe_{74}Co_{26}$	1.02	1.93×10^6	2.16
$Fe_{51}Co_{49}$	$Fe_{62}Co_{38}$	1.11	1.76×10^6	1.79
$Fe_{33}Co_{67}$	$Fe_{45}Co_{55}$	0.98	1.74×10^6	1.76

magnetic moment and their alignement for two different energy situations considering the longest (*2b*) and shortest (*2a*) distances between them. In our case, $\overrightarrow{m_1} = \overrightarrow{m_2} = \overrightarrow{m}$, and $r = 48$ or 4 nm (*2b* and *2a* distances, respectively). Taking the magnetization value of the $Fe_{exc}Co$ alloy, that is 2.36 T or 1.93 MA/m, we can easily derive values for the dipole interaction energy density for both cases. When magnetic dipoles are placed in configuration a) and just considering first neighbours interactions: $\approx$ - 63 kJ/m^3 for the longest (*2b*) distance (that is, moderate attractive interaction), and $\approx$ 27 MJ/m^3 for the shortest (*2a*) one (strong repulsive interaction).

However and when magnetic dipoles are placed in configuration b): still $\approx$ - 63 kJ/m^3 for the longest (*2b*) distance (that is, moderate attractive interaction), and $\approx$ - 27 MJ/m^3 for the shortest (*2a*) one (strong attractive interaction). So, most probably this last configuration is the most realistic one. These strong magnetic dipole interaction energy density values justify the observed agglomerates (TEM and AFM/MFM observations) of our synthesized Fe_xCo_{1-x} alloy nanoparticles, being those agglomerates in the origin of the observed hysteresis loops with low remanence-to-saturation (M_r / M_S) ratio [63].

4. Conclusions

In conclusion, we have successfully synthesized by using the chemical reduction route nanoparticles of pure Fe, pure Co and different high magnetization Fe_xCo_{100-x} alloy compositions: with Fe excess, equiatomic FeCo composition and with Co excess. The obtained final products of these pure Fe and Co and FeCo alloy nanoparticles shows high purity with no presence of any related oxide, as probed by NPD, EXAFS and Mössbauer nuclear techniques. This last technique also demonstrated that the FeCo alloy nanopowders are in an A2 type disordered solid solution. Room temperature magnetic measurements have determined values as high as 228 Am^2/kg for the Fe excess alloy, competing well even with values measured for the corresponding bulk alloy composition. These observed good soft magnetic properties are also accompanied by a long-time stability in air. AFM/MFM images have unveiled that these FeCo alloy nanoparticles shows small and "flaky" shape, of typical size of about 4 nm (thickness) x 50–60 nm (main diameter). This particular geometry of our NPs gives rise to a strong shape-anisotropy value, that is in the origin of the measured effective anisotropy constant K_{eff} values, in the range of 1–2 MJ/m^3.

CRediT authorship contribution statement

Inés Puente: Writing – review & editing, Methodology, Investigation. **Virginia Vadillo:** Validation, Methodology. **Jon Gutierrez:** Writing – original draft, Validation, Supervision, Investigation, Conceptualization. **Tommaso Baroni:** Writing – review & editing, Investigation, Formal analysis. **Izaskun Gil de Muro:** Methodology, Investigation, Formal analysis. **Joseba S. Garitaonandia:** Writing – review & editing, Validation, Methodology, Investigation. **Patricia Lázpita:** Writing – review & editing, Investigation, Formal analysis. **Iñaki Orue:** Writing – review & editing, Methodology, Investigation, Formal analysis. **Javier Alonso:** Methodology, Investigation, Formal analysis. **Marie Capron:** Writing – review & editing, Investigation, Formal analysis. **Claudia Mondelli:** Writing – review & editing, Methodology, Investigation. **Maite Insausti:** Writing – original draft, Supervision, Investigation, Funding acquisition, Conceptualization. **Francesco D'Acapito:** Writing – original draft, Investigation, Formal analysis.

Declaration of Competing Interest

The authors declare the following financial interests/personal relationships which may be considered as potential competing interests: J. Gutierrez reports financial support was provided by Spanish Ministry of
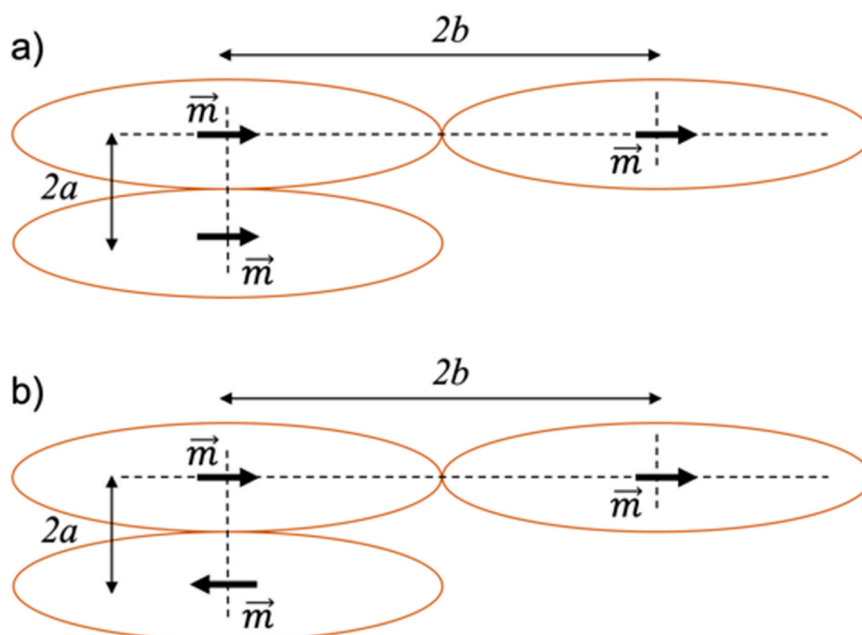
Fig. 13. Graphic representation of several Fe_xCo_{1-x} alloy single nanoparticles assumed as oblate spheroids, with long (*2b*) and short (*2a*) distances for magnetic dipolar interaction estimation.

Appendix A. Supporting information

Supplementary data associated with this article can be found in the online version at doi:10.1016/j.jallcom.2024.177211.

Data availability

Data will be made available on request.

References

[1] A. Ali, T. Shah, R. Ullah, P. Zhou, M. Guo, M. Ovais, Z. Tan, Y. Rui, Front. Chem. 9 (2021) 629054, https://doi.org/10.3389/fchem.2021.629054 (Article).
[2] E.M. Materon, C.M. Miyazaki, O. Carr, N. Joshi, P.H.S. Picciani, C.J. Dalmaschio, F. Davis, F.M. Shimizu, Appl. Surf. Sci. Adv. 6 (2021) 100163.
[3] Z. Ma, J. Mohapatra, K. Wei, J.Ping Liu, S. Sun, Chem. Rev. 123 (7) (2023) 3904, https://doi.org/10.1021/acs.chemrev.1c00860.
[4] N. Malhotra, J.S. Lee, R.A.D. Liman, J.M.S. Ruallo, O.B. Villaflores, T.R. Ger, C. D. Hsiao, Molecules 25 (2020) 3159, https://doi.org/10.3390/molecules25143159.
[5] Ö. Çelik, T. Fırat, J. Magn. Magn. Mat. 456 (2018) 11–16.
[6] J. Li, Z. Xi, Y.-T. Pan, J.S. Spendelow, P.N. Duchesne, D. Su, Q. Li, C. Yu, Z. Yin, B. Shen, J. Am. Chem. Soc. 140 (2018) 2926–2932.
[7] T. Sourmail, Prog. Mater. Sci. 50 (2005) 816–880.
[8] Ch Kuhrt, L. Schultz, J. Appl. Phys. 73 (1993) 6588.
[9] J.M. MacLaren, T.C. Schulthess, W.H. Butler, R. Sutton, M. McHenry, J. Appl. Phys. 85 (8) (1999) 4833.
[10] M. Ležaić, Ph Mavropoulos, S. Blügel, Appl. Phys. Lett. 90 (2007) 082504.
[11] I. Robinson, S. Zacchini, L.D. Tung, S. Maenosono, N.T.K. Thanh, Chem. Mater. 21 (2009) 3021–3026.
[12] N.O. Nuñez, P. Tartaj, M.P. Morales, P. Bonville, C.J. Serna, Chem. Mater. 16 (2004) 3119–3124.
[13] S. An, X. Li, W. Li, F. Ren, P. Xu, Mat. Lett. 284 (2021) 128965.
[14] V. Vadillo, A. Gómez, J. Berasategi, J. Gutiérrez, M. Insausti, I. Gil de Muro, J. S. Garitaonandia, A. Arbe, A. Iturrospe, M.M. Bou-Ali, J.M. Barandiarán, Soft Matter 17 (2021) 840–852, https://doi.org/10.1039/d0sm01702g.
[15] V. Vadillo, M. Insausti, J. Gutiérrez, J. Magn. Magn. Mater. 563 (2022) 169975, https://doi.org/10.1016/j.jmmm.2022.169975.
[16] J.M.D. Coey, Magnetism and Magnetic Materials, Cambridge University Press, 2010. ISBN: 978-0-521-81614-4.
[17] D. Lisjak, A. Mertelj, Prog. Mater. Sci. 95 (2018) 286–328.
[18] H. Khurshid, J. Alonso, Z. Nemati, M.H. Phan, P. Mukherjee, M.L. Fdez-Gubieda, J. M. Barandiarán, H. Srikanth, J. Appl. Phys. 117 (2015) 17A337.
[19] D.C. Koningsberger, R. Prins, X-ray Absorption: Principles, Applications, Techniques of EXAFS, SEXAFS and XANES, Wiley, New York, 1988.
[20] C.A. Schneider, W.S. Rasband, K.W. Eliceiri, NIH Image to ImageJ: 25 Years of Image Analysis, Nat. Methods 9 (2012) 671–675.
[21] U. Hartmann, Annu. Rev. Mater. Sci. 29 (1999) 53–87, https://doi.org/10.1146/annurev.matsci.29.1.53.
[22] H.M. Rietveld, J. Appl. Crystallogr. 2 (1969) 65–71.
[23] J. Rodríguez-Carvajal, Phys. B Condens. Matter 192 (1993) 55–69.
[24] Jon Gutiérrez, Julio Cuello Gabriel, Maite Insausti Peña, Vivian Nassif, Inés Puente Orench and Virginia vadillo Lacasa, Magn. Struct. Study High. Magn. FexCo1-x Nanopart. Magnetorheol. Fluids", Inst. Laue-Lange (ILL (2020), https://doi.org/10.5291/ILL-DATA.CRG-2782.
[25] F. d'Acapito, G.O. Lepore, A. Puri, A. Laloni, F. La Mannna, E. Dettona, A. De Luisa, A. Martin, The LISA beamline at ESRF, J. Synchrotron Radiat. 26 (2019) 551–558.
[26] R.A. Brand, Normos Mössbauer Fitting Program, Univ. Duisburg, 2002.
[27] S.B. Dalavi, M.M. Rajab, R.N. Panda, New J. Chem. 39 (2015) 9641–9649, https://doi.org/10.1039/c5nj01727k.

[28] A.A. Vasilev, E.L. Dzidziguri, M.I. Ivantsov, M.N. Efomiv, J. Phys.: Conf. Ser. 741 (2016) 012186, https://doi.org/10.1088/1742-6596/741/1/012186.

[29] E.A. Denisova, L.A. Chekanova, S.V. Komogortsev, I.V. Nemtsev, R.S. Iskhakov, M. V. Dolgopolova, J. Supercond. Nov. Magn. 34 (10) (2021) 05964.

[30] E.P. Yelsukov, E.V. Voronina, V.A. Barinov, J. Magn. Magn. Mater. 115 (1992) 27.

[31] S.G. Wang, Y. Mei, K. Long, Z.D. Zhang, Nanoscale Res. Lett. 5 (2010) 48–54, https://doi.org/10.1007/s11671-009-9441-4.

[32] M. Rahaman, Kungliga Tekniska Hogskolan; 2013; ⟨htttp://kth.diva-portal.org/smash/get/diva2:651507/FULLTEXT01.pdf⟩.

[33] M. Muralles, J.T. Oh, Z. Chen, J. Mater. Res. Technol. 19 (2022) 1102–1110.

[34] S.W. Van Sciver, Helium Cryogenics, Chapter 2: Low-Temperature Materials Properties, International Cryogenics Monograph Series; doi: 10.1007/978-1-4419-9979-5_2.

[35] B. Gehrmann, M. Acet, H.C. Herper, E.F. Wassermann, W. Pepperhoff, Phys. Status Solidi (b) 214 (1999) 175–185.

[36] Z. Rao, D. Ponge, F. Körmann, Y. Ikeda, O. Schneeweiss, M. Friak, J. Neugebauer, D. Raabe, Z. Li, Intermetallics 111 (11) (2019) 106520, https://doi.org/10.1016/j.intermet.2019.106520.

[37] P.A. Lee, P.H. Citrin, P. Eisenberger, B.M. Kincaid, Rev. Mod. Phys. 53 (1981) 769.

[38] B. Ravel, M. Newville, ATHENA and ARTEMIS: interactive graphical data analysis using IFEFFIT, Phy. Scr. T115 (2005) 1007.

[39] B. Ravel, ATOMS: crystallography for the X-ray absorption spectroscopist, J. Synchrotron Radiat. 8 (2001) 314.

[40] J.J. Rehr, R.C. Albers, S.I. Zabinsky, Phys. Rev. Lett. 69 (1992) 3397–3400.

[41] C. Maurizio, N. Michieli, B. Kalinic, A. Marafon, C. Scian, G. Mattei, Thin Solid Films 691 (2019) 137628.

[42] Atomic Calculation of Photoionization Cross-Sections and Asymmetry Parameters, ⟨https://vuo.elettra.eu/services/elements/WebElements.html⟩, [22/06/2022].

[43] F. Boscherini, S. De Panfilis, J. Weissmuller, Phys. Rev. B 57 (1998) 6.

[44] C. Maurizio, N. Michieli, B. Kalinic, V. Mattarello, V. Bello, F. Wilhelm, K. Ollefs, G. Mattei, Appl. Surf. Sci. 433 (2018) 596–601.

[45] A.M. Beale, B.M. Weckhuysen, Phys. Chem. Chem. Phys. 12 (2010) 5562–5574, https://doi.org/10.1039/b925206a.

[46] Z.J. Huba, K.J. Carroll, E.E. Carpenter, J. Appl. Phys. 109 (2011) 07B514.

[47] I. Castellanos-Rubio, O. Arriortua, L. Marcano, I. Rodrigo, D. Iglesias-Rojas, A. Barón, A. Olazagoiti-Garmendia, L. Olivi, F. Plazaola, M.L. Fernández-Gubieda, A. castellanos-Rubio, J.S. Garitaonandia, I. Orue, M. Insausti, Chem. Mater. 33 (2021) 3139–3154, https://doi.org/10.1021/acs.chemmater.0c04794.

[48] B.D. Cullity, C.D. Graham, Introduction to Magnetic Materials, IEEE Press & John Wiley & Sons Inc. Publication, 2009. ISBN: 978-0-471-47741-9.

[49] R. Skomski, J.M.D. Coey, Permanent Magnetism, Institute of Physics Publishing Ltd, Bristol and Philadelphia, 1999. ISBN: 07503-0478-2.

[50] I. Vincze, I.A. Campbell, J. Phys. F: Met. Phys. 3 (1973) 647–663, https://doi.org/10.1088/0305-4608/3/3/023.

[51] J. Chojcan, J. Alloy Compd. 264 (1998) 50–53, https://doi.org/10.1016/S0925-8388(02)00995-7.

[52] P. Eyméoud, P. Maugis, J. Magn. Magn. Mater. 513 (2020) 167223, https://doi.org/10.1016/j.jmmm.2020.167223.

[53] I. Vincze, I.A. Campbell, A.J. Mayer, Solid State Comm. 15 (1974) 1495–1499, https://doi.org/10.1016/0038-1098(74)90924-7.

[54] B. de Mayo, D.W. Foreter, S. Spooner, J. Appl. Phys. 41 (1970) 1319–1320, https://doi.org/10.1063/1.1658920.

[55] E.M.M. Ibrahim, S. Hampel, A.U.B. Wolter, M. Kath, A.A. El-Gendy, R. Klingeler, C. Tašchner, V.O. Khavrus, T. Gemming, A. Leonhardt, B. Büchner, J. Phys. Chem. C 116 (2012) 22509–22517.

[56] J. Bansmann, A. Kleibert, M. Getzlaff, A.Fraile Rodriguez, Frithjof Nolting, Christine Boeglin, Karl-Heinz Meiwes-Broer, Phys. Status Solidi B (2010) 247.

[57] T. Hasegawa, T. Niibori, Y. Takemasa, M. Oikawa, Sci. Rep. 9 (2019) 5248.

[58] T. Burkert, L. Nordström, O. Eriksson, O. Heinonen, Phys. Rev. Lett. 93 (4) (2004) 027203.

[59] S. Chikazumi. Physics of Ferromagnetism, 2nd Edition, Oxford University Press, New York, 1997. ISBN: 0-19-851776-9.

[60] E. Becker, H. Polley, Ann. Phys. 37 (1940) 534.

[61] 53-Herbst] J.F. Herbst, F.E. Pinkerton, Law of approach to saturation for polycrystalline ferromagnets: remanent initial state, Phys. Rev. B 57 (1998) 10733–10739.

[62] I. Arief, S. Biswas, S. Bose, ACS Appl. Mater. Interfaces 8 (2018) 26285–26297.

[63] R.P. Tan, J. Carrey, M. Respaud, Phys. Rev. B 90 (2014) 214421, https://doi.org/10.1103/PhysRevB.90.214421.

[64] S. Blundell, Magnetism in Condensed Matter, Oxford University Press Inc., New York, 2001. ISBN: 0-19-850592-2.